Error Rate Performance Analysis of the 5G NR Physical Uplink Shared Channels for Cell-Free Systems

Mostafa Rahmani[1], Junbo Zhao[1], Yi Chu[1], David Grace[1], Robert G Maunder[2], and Alister Burr[1]

[1]School of Physics, Engineering and Technology, University of York
[2]University of Southampton

December 11, 2024

Error Rate Performance Analysis of the 5G NR Physical Uplink Shared Channels for Cell-Free Systems

Mostafa Rahmani*, Junbo Zhao*, Yi Chu*, David Grace*,
Robert G Maunder†, Alister Burr*
*School of Physics, Engineering and Technology, University of York, UK, †University of Southampton, UK

***Abstract*—This paper investigates the physical layer performance of 5G New Radio (NR) in a cell-free (CF) massive MIMO system, focusing on the transmission of the Physical Uplink Shared Channel (PUSCH) over frequency-selective Rayleigh fading channels. A comprehensive link-level simulator, compliant with 3GPP standards, is developed to evaluate the system's performance across various scenarios. Key parameters such as subcarrier spacing (SCS), modulation and coding schemes (MCS) (QPSK, 16-QAM, 64-QAM, 256-QAM), and varying numbers of distributed radio units (RUs) are systematically analyzed. The results demonstrate the dual benefits of increasing the number of RUs: enhanced spatial diversity and improved proximity between user equipment (UE) and RUs, leading to significant improvements in reliability and error rate performance. The study also highlights the impact of higher SCS values in leveraging frequency diversity, particularly when signal bandwidth exceeds the channel's coherence bandwidth. Practical channel estimation is incorporated to validate performance under realistic conditions. Block Error Ratio (BLER) is used as the primary performance metric, providing valuable insights into the interplay of spatial and frequency diversity in CF 5G NR systems, thereby confirming their potential to achieve robust and efficient communication in challenging wireless environments.**

***Index Terms*—Cell-free system, Block error rate, Physical uplink shared channel, 5G New Radio.**

I. Introduction

With next-generation demands for higher data rates, broader coverage, and enhanced user experience, cell-free multiple-input multiple-output (CF-MIMO) technology is emerging as a key solution. Unlike traditional cellular networks, CF-MIMO effectively removes cell boundaries, creating a cooperative network of access points (APs) that collectively serve all user equipment (UE). This design improves coverage and throughput, particularly at network edges, by leveraging macro-diversity. In CF-MIMO, distributed APs connect to a central processing unit (CPU) through a fronthaul network for synchronized transmission and reception, enhancing signal quality (SNR and SINR) network-wide [1]. Alongside CF-MIMO, 5G New Radio (NR) technology, developed by the Third Generation Partnership Project (3GPP), has progressed rapidly [2].

CF-MIMO architectures have garnered significant research interest over the past decade, establishing foundational elements such as uplink and downlink operation, pilot assignment, pilot decontamination, channel estimation, and power control algorithms [3]–[6]. However, most studies have assumed single-carrier transmission, which is appropriate for block-wise frequency-flat, time-invariant fading channels, where the channel fading remains constant across the entire time-frequency resource grid. While this assumption simplifies analysis and can provide accurate approximations when RBs fit within the channel's coherence bandwidth and time, real-world wireless channels are inherently frequency-selective and time-varying.

Research on CF-MIMO systems that accounts for bandwidth and frequency-selective channels is still sparse. Only few studies address performance in frequency-selective channels, with channel aging and phase noise examined in limited works. Zheng et al. [7] provided closed-form uplink and downlink rate expressions that consider channel aging, spatial correlation, and pilot contamination, showing that CF-MIMO is more resilient to channel aging than small cell systems. In [8], Jiang et al. investigate how channel aging and phase noise affect the performance of zero-forcing precoding in CF-MIMO systems. They argue that the exchange of channel state information (CSI) and precoded data over a fronthaul network incurs considerable delay, which necessitates the use of delay-aware techniques like channel prediction to mitigate its impact.

In [9], the authors investigate the effects of frequency-selective fading channels on the design and performance of CF-MIMO orthogonal frquency-division multiplexing (CF-MIMO-OFDM) networks, providing a comprehensive characterization of time and frequency selectivity as well as intercarrier interference. Furthermore, an innovative opportunistic AP selection scheme aimed at enhancing time-frequency resource utilization in a CF-MIMO-OFDM system was introduced in [10]. The approach assigns subcarriers orthogonally to users, ensuring only one user per subcarrier, and serves each user only through nearby APs while deactivating distant APs to reduce power wastage on high-loss channels. This selective activation reduces the number of active APs per subcarrier, enabling feasible downlink pilot use and coherent detection.

In [11] the performance of CF-MIMO-OFDM systems in high-speed train communications is analyzed, considering fully centralized and local minimum mean square error (MMSE) combining. The study derives closed-form expressions for uplink spectral efficiency, accounting for local

The work presented in this paper was funded by UK Department for Science, Innovation and Technology under projects YO-RAN and DU-Volution .

maximum ratio combining, large-scale fading decoding cooperation, and the impact of Doppler frequency offset on system performance. Building on these insights, our study examines practical channel estimation effects and compares them with ideal channel estimation to assess realistic performance bounds in CF architectures. In [12] OFDM-based multicarrier transmission approach for CF-MIMO systems over frequency-selective fading channels is presented and analyzed. The study proposes frequency-domain conjugate beamforming, pilot assignment, and user-specific resource allocation strategies to enhance system performance. Additionally, the method of superimposed pilots for channel estimation in CF-MIMO-OFDM systems has been investigated and documented in [13].

While most research on CF-MIMO systems has focused on evaluating spectral efficiency and energy efficiency, other vital performance metrics, such as outage probability (OP) and error performance analysis, have been relatively underexplored. These metrics are crucial for assessing system reliability in real-world scenarios. Determining a closed-form expression for OP is particularly challenging due to the complex nature of CF-MIMO systems [14]. In [15], a closed-form expression for the OP in full-duplex CF-MIMO systems is derived and verified using analytical approaches and simulations, including an analysis of asymptotic performance. The study considers the effects of imperfect CSI and user mobility, allowing multiple user equipments (UEs) to operate on shared spectrum resources.

To the best of the authors' knowledge, no prior research has examined the implementation CF-MIMO systems based on 5G NR with Physical Uplink Shared Channel (PUSCH) fully aligned to 3GPP standards. While CF-MIMO systems have been widely studied in theoretical contexts, existing works often rely on simplified or custom waveform and protocol assumptions, diverging from practical 3GPP-compliant architectures. This gap underscores the significance of this study, which aims to bridge theory and practice by leveraging the standardized 5G NR framework. Such alignment not only ensures interoperability with existing networks but also provides a realistic foundation for evaluating CF-MIMO systems in real-world deployment scenarios.

This study contributes to addressing this gap by providing simulation results grounded in the 5G NR air interface. A focal point of this work is the analysis of Block Error Rate (BLER), a key metric for assessing link quality in modern communication systems. BLER is especially significant in 5G networks, where adaptive modulation, coding, and resource allocation strategies depend on maintaining target BLER thresholds as defined in 3GPP TS 23.501. These thresholds are tailored to meet the stringent quality of service (QoS) requirements of diverse applications, ranging from ultra-reliable low-latency communication to enhanced mobile broadband.

Despite its importance, the exploration of BLER performance in CF-MIMO-OFDM systems remains limited in existing literature, with most studies focusing on traditional setups that overlook the distributed nature and unique architectural characteristics of CF-MIMO. By analyzing BLER curves within the CF-MIMO-OFDM framework, this paper provides critical insights into the interaction of distributed MIMO architectures with 5G NR air interfaces, aiming to establish a foundational understanding of how CF-MIMO can deliver reliable and efficient communication in real-world scenarios. The findings highlight its potential to meet the diverse and demanding requirements of next-generation wireless networks. Notably, the comparative analysis reveals that different UEs within the same CF-MIMO system exhibit varying slopes in their BLER versus SNR performance, despite sharing the same frequency bandwidth, being served by the same RUs, and affected by the same channel conditions. This variation underscores the complexity and dynamic behavior of CF-MIMO systems, emphasizing the need for further investigation. Understanding these differences could offer valuable insights into optimizing QoS distribution and ensuring equitable service reliability across all UEs in the network. The main contributions of this study are summarized as follows:

1. We design a link-level simulator tailored for an uplink CF-MIMO system, incorporating all the PUSCH processing procedures as defined by the 3GPP standards for 5G NR. BLER is employed as a primary metric to evaluate and compare system performance across different setups. This approach provides meaningful insights into reliability under various configurations.
2. We examine the impact of crucial parameters, including different sub-carrier spacings, varying numbers of RUs, and different modulation schemes: quadrature phase shift keying (QPSK), 16 quadrature amplitude modulation (16-QAM), 64-QAM, 256-QAM.
3. We investigate the interplay between frequency-selective channels and the CF architecture, demonstrating how the combination of spatial and frequency diversity enhances resource exploitation and ensures consistent performance across users and channel conditions. This focus provides critical insights into the potential of CF-MIMO systems to address fading and improve reliability in next-generation wireless networks.
4. We investigate the effects of practical channel estimation by comparing it with ideal (perfect) channel estimation, demonstrating the performance implications of realistic channel estimation in a CF-MIMO system.

The rest of the paper is organized as follows: In Section II, we first present a brief overview of 5G NR PUSCH, followed by the proposed structure of a 5G-based link-level simulator for CF-MIMO systems. Section III describes the system and channel models, and also the UL training and payload data transmission phase. The BLER analysis of the CF-MIMO system is studied in Section IV by considering all the performance metrics. Finally, conclusions are drawn, and future work is discussed in Section VI.

Notation: We will adopt the following notations in the rest of the paper. The superscripts $()^*$, $()^{\mathrm{T}}$ and $()^{\mathrm{H}}$ represents the complex conjugate, transpose, and conjugate-transpose, respectively. An uppercase boldface letter stands for a matrix or a vector with the elements in the frequency domain, while a lowercase boldface letter represents a vector in the time domain.

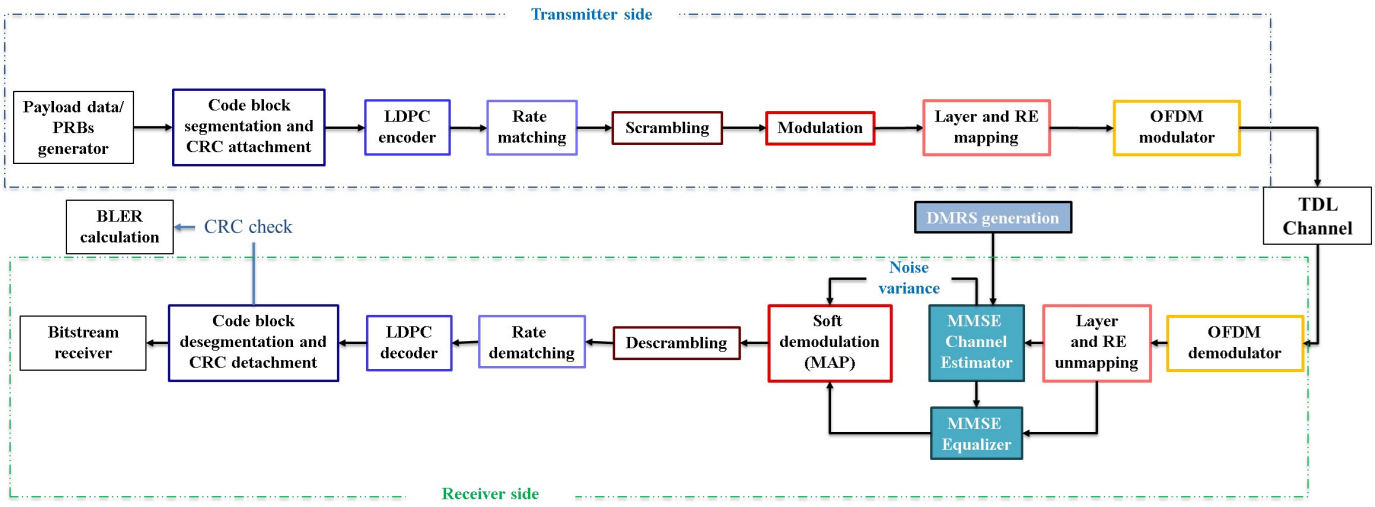

Fig. 1. Transmitter and receiver chain of the 5G NR PUSCH channel.

II. PRELIMINARIES FOR 5G-BASED LINK-LEVEL SIMULATOR

This section is organized into three subsections, each addressing a key aspect of the link level simulator. Subsection II-A outlines the core principles of 5G NR, emphasizing the PUSCH processing. Subsection II-B discusses the alignment of CF-MIMO systems with O-RAN architecture, and subsection II-C details the simulator's workflow, from UE payload transmission through a modeled channel to centralized DU processing, including channel estimation, equalization, decoding, and error calculation.

A. 5G New Radio

Selecting an appropriate radio waveform is crucial for mobile access technologies, as it significantly impacts system performance [16]. In 5G NR, OFDM with Cyclic Prefix (CP-OFDM) is adopted for both downlink and uplink transmissions, as recommended by 3GPP. This choice is due to CP-OFDM's low implementation complexity, cost-effectiveness for wide bandwidths, and MIMO systems.

Fig.1 illustrates the physical layer processing of the 5G NR PUSCH including transmitter and receiver chains [17]. The PUSCH processing at the transmitter side consists of several steps: first, a Cyclic Redundancy Check (CRC) is added to the payload for error detection. The payload is then segmented into code blocks, which are individually encoded using Low-Density Parity-Check (LDPC) coding, tailored to the payload size. Following LDPC encoding, rate matching is performed to adjust the coding rate to match the channel capacity. The resulting code blocks are concatenated into a single codeword, which is subsequently scrambled and modulated using the QPSK, 16-QAM, 64-QAM, or 256-QAM modulation, depending on the PUSCH requirements. The modulated symbols are then layer-mapped according to the available antenna ports, followed by precoding for transmission. Finally, the symbols are mapped to the resource grid, ensuring efficient allocation of frequency and time resources for OFDM signal generation, ready for transmission over the channel.

The receiver processing chain in 5G NR starts with the OFDM demodulator, which converts the received time-domain signal into the frequency domain and removes the cyclic prefix. The demodulated signal is then layer and RE unmapped to separate signals from multiple layers and align them with their corresponding Resource Elements (REs). MMSE channel estimation is performed using Demodulation Reference Signal (DMRS) to derive CSI, followed by MMSE equalization to mitigate channel fading and interference.

The equalized data undergoes soft demodulation, converting the symbols into Log-Likelihood Ratios, which are then descrambled to restore the original encoded sequence. Rate dematching reverses the rate matching process, restoring the encoded sequence length, which is then passed to the LDPC decoder for error correction. The decoded data is desegmented, and the CRC is detached and checked for errors. Finally, the error-checked data is passed to the bitstream receiver, and the BLER calculation evaluates the overall system performance. This structured process ensures reliable recovery of transmitted data in complex wireless environments.

B. Cell-Free System in O-RAN Networks

CF-MIMO systems require fine-grained processing flexibility, such as task allocation between APs and CPUs, and this aligns naturally with the Open Radio Access Networks (O-RAN) disaggregation concept. O-RAN, standardizes RAN functionality through its architecture, which separates the radio access network into the central unit (CU), distributed unit (DU), and radio unit (RU). Within this framework, the CPU in CF-MIMO systems corresponds to the DU, and APs correspond to RUs, enabling better alignment of CF-MIMO system with industry standards. The O-RAN 7-2x functional split divides the physical layer processing between DUs and RUs, balancing simplicity in RUs with fronthaul efficiency. This architectural alignment facilitates practical CF implementations, leveraging O-RAN's standardized framework to advance CF-MIMO systems in real-world deployments [18].

C. Cell-free link-level simulator

Fig. 2 presents a block diagram of a link-level simulator designed for a CF-MIMO system comprising M RUs and K UEs. Each RU and UE is equipped with a single antenna, with their positions randomly distributed across a large area. All M RUs are connected to a DU via fronthaul links. The DU manages and coordinates physical layer signal processing and medium access control (MAC) for all RUs. On the **UE Side**, each UE transmits its data payload (e.g., Payload 1 for UE 1, Payload k for UE k) through an uplink process that includes UL-SCH processing, followed by PUSCH encoding, and CP-OFDM modulation. These steps prepare the data for transmission over the uplink channel, converting it into a suitable format for propagation. It should be mention that all UEs transmit in the same time-frequency resources and that they interfere in the channel.

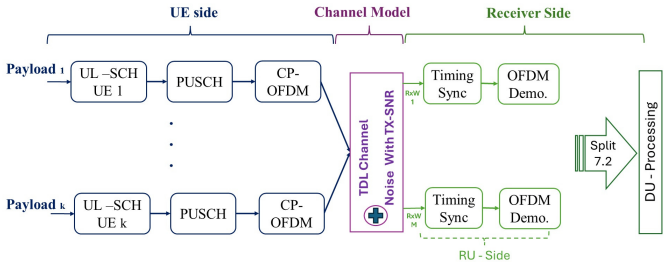

Fig. 2. Block diagram of link-level simulator for Cell-free system.

The **Channel Model** represents the wireless propagation environment between the UEs and RUs. Here, each transmitted signal undergoes transmission through a TDL (Tapped Delay Line) channel model, which simulates realistic multi-path effects, including reflections and delays, and introduces noise with a specified transmit signal-to-noise ratio (TX-SNR). This step emulates real-world signal degradation, interference, and other channel impairments.

On the **Receiver Side**, each RU receives the transmitted signals with added channel effects and noise, represented by RxW_1 to RxW_M, indicating the received signals at each RU. These received signals are then processed to achieve timing synchronization ("Timing Sync") and OFDM demodulation ("OFDM Demod."), which reverses the CP-OFDM modulation applied on the UE side to retrieve the original transmitted data. This process is performed for each RU independently, allowing simultaneous data reception from multiple UEs.

Finally, all processed signals are forwarded to the DU for centralized processing. This stage includes **DU Processing**, where advanced signal processing and decoding are carried out to manage interference and optimize resource allocation. The functional split, labeled **Split 7.2**, denotes the division of processing responsibilities between the RUs and the DU, a design strategy for efficient data handling and coordination across multiple RUs. This structure allows all M RUs to serve all K UEs simultaneously within the same time-frequency resource, which is a defining characteristic of CF-MIMO systems.

Fig 3 illustrates the detailed stages of DU processing for the CF link-level simulator. In this architecture the DU

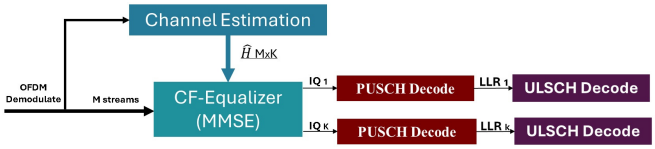

Fig. 3. DU Processing Stages in Cell-Free Link-Level Simulator

processing includes essential tasks such as channel estimation, equalization, demapping, and LDPC decoding. Demodulated signals from each of the M RUs are transmitted as M parallel streams to the DU, where centralized processing begins on these streams. Next, in the **Channel Estimation** block, channel estimation is performed to determine the channel response matrix $\hat{H}_{M\times K}$, where M is the number of RUs and K represents the number of UEs. Channel estimation is crucial in CF-MIMO systems as it provides the necessary information to compensate the effects of the wireless channel and interference.

Following channel estimation, the signal passes through the **CF-Equalizer (MMSE)** block. Here, a CF equalizer with MMSE criteria is applied to minimize the residual interference and noise. The equalizer uses the estimated channel matrix $\hat{H}_{M\times K}$ to improve signal quality by adjusting the received signals for each user (indicated as IQ_1 to IQ_K). This equalization is particularly effective in CF-MIMO systems where multiple RUs serve all UEs with the same radio resource.

After equalization, the data is forwarded to the **PUSCH Decode** blocks (also known as soft demdulator), which performs inverse processing as specified in [19, Section 6.3.1], returning soft bits in the form of LLR. The decoding process includes layer demapping, symbol demodulation using the modulation scheme, and descrambling. This step prepares the signal for the subsequent decoding phase.

Finally, the output of the PUSCH Decode is fed into the **ULSCH Decode** blocks. ULSCH decoding performs error correction on the bit streams, which helps recover the original data by correcting errors that occurred during transmission. LDPC codes are highly efficient for handling large data blocks in modern wireless systems and are essential for ensuring reliable communication in high-performance, CF-MIMO systems.

Overall, these diagrams represent the comprehensive workflow of the link-level simulator, simulating data transmission from UEs through a shared channel environment, signal reception and synchronization at the RUs, and centralized processing at the DU for efficient CF communication.

III. System Model

The section is organized into five subsections that collectively explain the components and processes of the uplink data transmission and channel estimation in 5G NR-based systems. Subsection III-A introduces the flexible time-frequency organization of 5G NR. Subsequently, Subsection III-B details the channel, modeled as a tapped delay line to account for multipath propagation effects. Following this, Subsection III-C explains the OFDM-based transmission process. Furthermore, Subsection III-D focuses on the use of DMRS for channel

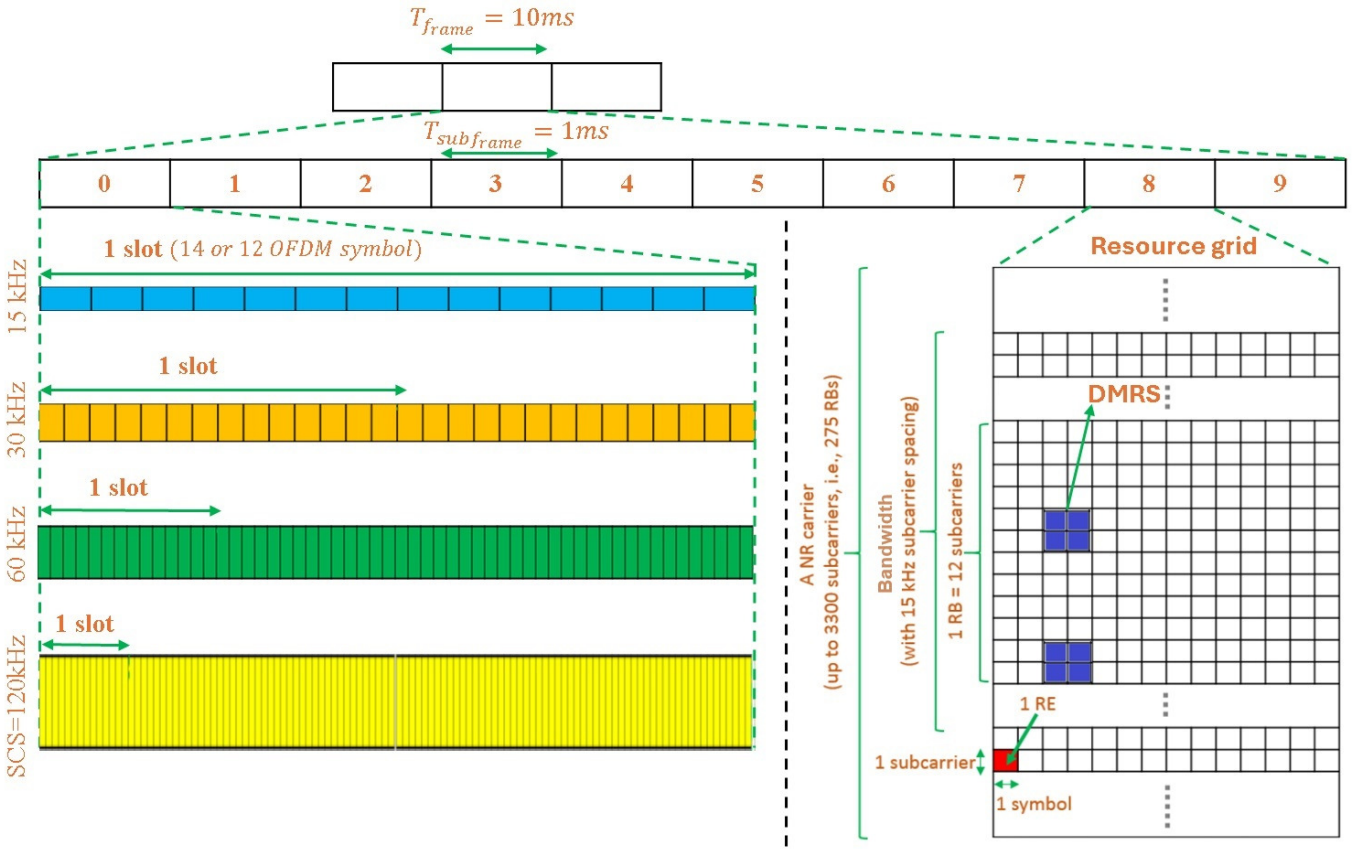

Fig. 4. Illustration of 5G NR transmission structure in time and frequency domain by considering four different subcarrier spacing [2].

estimation. Finally, Subsection III-E describes the Uplink data transmission.

A. Frame and Pilot Structure

In 5G NR, uplink (and downlink) data transmission is organized into 10 ms frames, each divided into 10 subframes of 1 ms. Each subframe consists of a variable number of slots, depending on the selected subcarrier spacing Δf, allowing flexibility. In the normal case, a slot contains 14 OFDM symbols, each with a cyclic prefix, whereas in the extended cyclic prefix (CP) option, a slot contains 12 OFDM symbols with a longer cyclic prefix. The smallest unit, a RE, is a subcarrier within the passband, and 12 consecutive REs in the same symbol form a Physical Resource Block (PRB). This flexible frame structure, as shown in Fig. 4, enables 5G NR to meet diverse requirements for cell size, latency, and interference resilience [17].

The 5G NR standard defines two types of reference signals associated with the transmission of the PUSCH channel. The DMRS is a user-specific reference signal with high frequency density, dedicated for frequency-selective channel estimation [20, Sec. 6.4.1.1]. It occupies specific OFDM symbols within each slot, with the number of OFDM symbols containing DMRS varying between 1 and 4 depending on the configuration. For rapidly changing channels, a higher density of DMRS symbols in time helps obtain more accurate channel estimates within the coherence time. In the frequency domain, DMRS symbols are mapped across the entire set of PRBs allocated to the PUSCH, and the spacing between DMRS REs assigned to the same RU can be set to 2 or 3 RE. In this work, we consider only DMRS for channel estimation.

B. Channel Model

Unlike previous research that assumes a flat-fading channel, this study adopts a more comprehensive approach by considering a channel model that is both time-selective and frequency-selective, making it suitable for analyzing broadband scenarios and capturing the dynamic behavior of real-world wireless channels. In practice, the channel fading is frequency selective, and can be modelled as a tapped delay line $\mathbf{h} = [h_0, \ldots, h_{L_{mk}-1}]^{\mathrm{T}}$, where L_{mk} is the number of multipath channel taps for the link between the k-th UE and the m-th RU. The normalized delay and corresponding power for the tapped delay line model is provided by 3GPP [21, Sec. 7.7.2]. The channel coefficient between the k-th UE and the m-th RU is then given by

$$\mathbf{g}_{mk} = [g_{mk,0}, \ldots, g_{mk,L_{mk}-1}]^{\mathrm{T}} = \sqrt{\beta_{mk}}\mathbf{h} \qquad (1)$$

where β_{mk} is the large-scale fading coefficient, as detailed in Section IV-B.

C. Signal Model

We define the N-point transmission block for a single OFDM symbol sent by the k-th UE as $\mathbf{X}_k = [X_{k,0}, \ldots, X_{k,N-1}]^{\mathrm{T}}$. Through the OFDM modulation, the

time domain sequence is given by $\mathbf{x}_k = [x_{k,0}, \ldots, x_{k,N-1}]^{\mathrm{T}}$ in which the *i*-th element is $x_{k,i} = \frac{1}{N}\sum_{n=0}^{N-1} X_{k,n} e^{2\pi j \frac{ni}{N}}$, where $i = 0, 1, \ldots, N-1$ and j denotes the imaginary unit. The sequence can also be written in matrix form as

$$\mathbf{x}_k = \frac{1}{N}\mathbf{F}_N^* \mathbf{X}_k \tag{2}$$

where $\mathbf{F}_N$ is the $N \times N$ discrete Fourier transform (DFT) matrix. Also, the CP is added to avoid inter-symbol interference (ISI), leading to the sequences $\mathbf{x}_k^{\mathrm{cp}}$. Through the multipath fading channel, the received signal at the *m*-th RU is given by $\mathbf{y}_m^{\mathrm{cp}} = \sum_{k=1}^{K} \mathbf{x}_k^{\mathrm{cp}} * \mathbf{g}_{mk} + \mathbf{z}_m^{\mathrm{cp}}$, where * denotes the linear convolution and $\mathbf{z}_m^{\mathrm{cp}}$ is the complex additive white Gaussian noise (AWGN) with the variance σ_z^2. Before doing the OFDM demodulation, the received signal should cut the residual tails and remove the CP in order to keep the same length as the OFDM modulated signals. This process can be expressed by [12]

$$\mathbf{y}_m = \sum_{k=1}^{K} \mathbf{g}_{mk}^N \otimes \mathbf{x}_k + \mathbf{z}_m \tag{3}$$

where $\otimes$ denotes the cyclic convolution, $\mathbf{z}_m$ is the part of the noise with size *N*, and $\mathbf{g}_{mk}^N$ is an *N*-point channel impulse response formed by padding zeros for $\mathbf{g}_{mk}$. The OFDM demodulated signal is given by

$$\begin{aligned} \mathbf{Y}_m = \mathbf{F}_N \mathbf{y}_m &= \sum_{k=1}^{K} \mathbf{F}_N (\mathbf{g}_{mk}^N \otimes \mathbf{x}_k) + \mathbf{F}_N \mathbf{z}_m \\ &= \sum_{k=1}^{K} \mathbf{G}_{mk} \odot \mathbf{X}_k + \mathbf{Z}_m \end{aligned} \tag{4}$$

where $\odot$ represents the Hadamard product, $\mathbf{G}_{mk} \in \mathbb{C}^{N\times 1}$ denotes the frequency response of $\mathbf{g}_{mk}^N$, and $\mathbf{Z}_m$ is the OFDM demodulation of $\mathbf{z}_m$ which has the variance σ_Z^2. Note that the variance of each element in the frequency domain differs from that in the time domain. The equation (4) demonstrates that the data transmission through a frequency-selective channel can be transformed into traversing a set of independent flat-fading subcarriers by adopting an OFDM system. It is worth mentioning that, here, we assume that the length of the channel's tapped delay line is shorter than the length of the cyclic prefix. The uplink transmission on the *n*-th subcarrier received at the *m*-th RU is then expressed as

$$Y_{m,n} = \sum_{k=1}^{K} G_{mk,n} X_{k,n} + Z_{m,n} \tag{5}$$

where $G_{mk,n}$, $X_{k,n}$ and $Z_{m,n}$ denote the *n*-th subcarrier, transmitted signal and noise in a single OFDM symbol in the frequency domain, respectively. To recover the data symbol, the uplink channel should be estimated for each sub-carrier.

D. Pilot Transmission and Channel Estimation

As mentioned earlier, the DMRS associated with the UL PUSCH transmission enables coherent demodulation of user data in the uplink. In 5G NR, four different categories of DMRS configurations are defined based on type (Type 1 and Type 2) and length (length 1 and length 2), and here we consider Type 2 and length 2, where DMRS symbols are inserted at the 3rd and 4th OFDM symbols, as shown in Fig. 4. The sequence that generates the DMRS symbols is $r(n)$, is defined as follows [22]

$$r(n) = \frac{1}{\sqrt{2}}(1 - 2\cdot c(2n)) + j\cdot\frac{1}{\sqrt{2}}(1 - 2\cdot c(2n+1)) \tag{6}$$

This is evidently a QPSK modulation scheme, where each symbol is mapped to one of the four constellation points $\left(\pm\frac{1}{\sqrt{2}} \pm j\frac{1}{\sqrt{2}}\right)$ based on a pseudo-random binary sequence $c(n)$. The pseudo-random sequence $c(n)$ is defined in [19, clause 5.2.1].

In a multi-user scenario, DMRS leverages a combination of frequency and code orthogonality to support efficient channel estimation. Code orthogonality is achieved through the use of Orthogonal Cover Codes (OCCs), which employ Walsh sequences to distribute the pilot signal across neighboring time and frequency REs. This approach is referred to as CDM-Multiplexed DM-RS in the 5G NR standards [23].

We assume that DMRS for the *k*-th UE is represented by a vector $\mathbf{P}_k \in \mathbb{C}^{N_p\times 1}$, where each DMRS vector is orthogonal to the others. The received DMRS at the m^{th} RU are then given by

$$\mathbf{Y}_m^{\mathrm{p}} = \sum_{k=1}^{K} \mathrm{diag}(\mathbf{P}_k)\mathbf{I}_{\mathrm{p}}\mathbf{G}_{mk} + \mathbf{Z}_m^{\mathrm{p}} \tag{7}$$

where $\mathrm{diag}(\mathbf{P}_{\mathrm{k}})$ denotes a diagonal matrix with the vector $\mathbf{P}_k$ placed on its diagonal (size $N_{\mathrm{p}} \times N_{\mathrm{p}}$). $\mathbf{I}_{\mathrm{p}}$ is an $N_{\mathrm{p}} \times N$ pilot indicator matrix in which the *i*-th row contains one at the position corresponding to the RE where the *i*-th pilot occurs, zero elsewhere. $\mathbf{Z}_m^{\mathrm{p}}$ represents the vector of noise in the pilot positions.

The least squares channel estimates in DMRS positions are calculated by

$$\begin{aligned} \hat{\mathbf{G}}_{mk} &= \left[\mathrm{diag}(\mathbf{P}_k)\right]^{-1} \overbrace{\left(\sum_{k'=1}^{K} \mathrm{diag}(\mathbf{P}_{k'})\mathbf{I}_{\mathrm{p}}\mathbf{G}_{mk'} + \mathbf{Z}_m^{\mathrm{p}}\right)}^{\mathbf{Y}_m^{\mathrm{p}}} \\ &= \mathbf{I}_{\mathrm{p}}\mathbf{G}_{mk} + \sum_{k'\neq k}^{K} \mathbf{\Theta}_{kk'}\mathbf{I}_{\mathrm{p}}\mathbf{G}_{mk'} + \boldsymbol{\zeta}_m. \end{aligned} \tag{8}$$

where $\mathbf{\Theta}_{kk'} = [\mathrm{diag}(\mathbf{P}_k)]^{-1}\mathrm{diag}(\mathbf{P}_{k'})$ is a diagonal matrix and the weighted noise denotes $\boldsymbol{\zeta}_m = [\mathrm{diag}(\mathbf{P}_k)]^{-1}\mathbf{Z}_m^{\mathrm{p}}$.

This limited-length channel estimate can be expanded to all sub-carriers and 14 OFDM symbols within a single resource grid through interpolation. When the DMRS occupies two OFDM symbols (with a DMRS length of two), the same equations (7) and (8) are used to obtain the channel estimates for both OFDM symbols. To estimate the channels for the full resource grid, interpolation is first applied across all sub-carriers. Then, using the channel estimates obtained from the two OFDM symbols, interpolation is extended over the time domain to cover all 14 OFDM symbols.

E. Uplink Data Transmission

On the uplink, we suppose the *k*-th UE transmits the PUSCH modulated symbol $S_{k,n}$, $\sigma_S^2 = \mathbb{E}\{|S_{k,n}|^2\} = 1$, with the power p_k on the *n*-th subcarrier. Substituting $X_{k,n} = \sqrt{p_k} S_{k,n}$ into (4), the received signal in the *n*-th RE at the *m*-th RU is

$$Y_{m,n} = \sqrt{p_k} \sum_{k=1}^{K} G_{mk,n} S_{k,n} + Z_{m,n} \tag{9}$$

Subsequently, the received signals from all *M* RUs are collected at the DU for equalization. By adopting combining techniques and channel estimation, the estimated PUSCH modulated symbols $\hat{S}_{k,n}$ transmitted from the *k*-th UE through the *n*-th subcarrier is calculated by

$$\begin{aligned}\hat{S}_{k,n} = \mathbf{W}_{k,n}\mathbf{Y}_n = \sqrt{p_k}\mathbf{W}_{k,n}\mathbf{G}_{k,n}S_{k,n} \\ + \sum_{i\neq k}^{K} \sqrt{p_i}\mathbf{W}_{k,n}\mathbf{G}_{i,n}S_{i,n} + \mathbf{W}_{k,n}\mathbf{Z}_n\end{aligned}$$

where $\mathbf{W}_{k,n} \in \mathbb{C}^{1\times M}$ is the weight vector decided by different combining techniques, $\mathbf{Y}_n = [Y_{1,n}, \ldots, Y_{M,n}]^{\mathrm{T}}$ represents the received signals of *M* RUs on the *n*-th subcarrier, $\mathbf{G}_{k,n} = [G_{1k,n}, \ldots, G_{Mk,n}]^{\mathrm{T}}$, and the noise vector $\mathbf{Z}_n = [Z_{1,n}, \ldots, Z_{M,n}]^{\mathrm{T}}$. The MMSE combining vector for the CF-Equalizer in Fig. 3 is given by

$$\mathbf{W}_{k,n} = \sqrt{p_k}\mathbf{G}_{k,n}^{\mathrm{H}} \left(\sum_{i=1}^{K} p_i \mathbf{G}_{i,n}\mathbf{G}_{i,n}^{\mathrm{H}} + \frac{\sigma_Z^2}{\sigma_S^2}\mathbf{I}_M \right)^{-1} \tag{10}$$

where $\mathbf{I}_M$ is the identity matrix with the size *M*.

Finally, the data is successfully recovered through a detailed process that involves PUSCH Decode and ULSCH Decode, both of which are implemented using the MATLAB 5G Toolbox.

IV. Numerical Results and Discussions

This section analyzes the influence of key parameters on the performance of the CF-MIMO system. The parameters under consideration include the number of RUs (2 RUs, 4 RUs, or 8 RUs), SCS values (15 kHz, 30 kHz, 60 kHz, 120 kHz), the type of channel estimation (CE) method employed—either perfect or practical—and the MCS. Unless explicitly specified otherwise, the results presented in this section are based on configurations with 8 RUs and an SCS of 15 kHz. The link-level performance is evaluated using BLER versus TX-SNR curves. These curves are generated by varying the average TX-SNR and measuring the BLER corresponding to each average SNR value, where the SNR range is a configurable parameter within our simulation framework. The BLER is defined as the ratio of incorrectly received blocks to the total number of transmissions. To ensure statistical accuracy in the reported results, simulations were conducted for 2×10^5 transport block (TB) transmissions for each average TX-SNR value, with the TDL channel being randomly varied for each TB. This approach ensures a sufficiently large number of independent channel realizations, resulting in reliable and representative performance metrics.

A. TX-SNR Definition

In uplink CF-MIMO systems, signals from a UE are received at multiple RUs over links with varying lengths and different path-losses, complicating the definition of a standard SNR. Therefore, the TX-SNR is used to plot BLER curves, defined as the ratio of the transmit power per UE antenna per RE to the noise power at the receivers. It is assumed that the transmit power is uniform across all transmitters, and the noise power is defined to achieve a specified TX-SNR.

B. Large-Scale Fading Model

The 3GPP path loss model and uncorrelated shadow fading in [21] are applied to calculate the large-scale fading coefficient β_{mk} in (1)

$$\beta_{mk} = 10^{\frac{\mathrm{PL}_{mk}+\mathrm{SF}_{mk}}{10}} \tag{11}$$

where PL_{mk} denotes the path loss, and $\mathrm{SF}_{mk} \sim \mathcal{N}(0, \sigma_{SF}^2)$ is the shadow fading. We consider a urban microcell (UMi) scenario with the non-line-of-sight (NLOS) propagation, in which the height of the RU antenna $h_{RU} = 10$ m, the height of UE antenna $h_{UE} = 1.65$ m and the carrier frequency $f_c = 1.9$ GHz. The path loss in dB is given by [21]

$$\mathrm{PL}_{mk} = \max(\mathrm{PL}_{mk,LOS}, \mathrm{PL}_{mk,NLOS}) \tag{12}$$

where

$$\begin{aligned}\mathrm{PL}_{mk,NLOS} = 35.3\log_{10}(d_{mk,3D}) + 22.4 \\ + 21.3\log_{10}(f_c) - 0.3(h_{UE} - 1.5)\end{aligned} \tag{13}$$

and

$$\mathrm{PL}_{mk,LOS} = \begin{cases} \mathrm{PL}_1 & 10\mathrm{m} \le d_{mk,2D} \le d_{BP}^{'} \\ \mathrm{PL}_2 & d_{BP}^{'} \le d_{mk,2D} \le 5\mathrm{km} \end{cases} \tag{14}$$

where $\mathrm{PL}_1 = 32.4 + 21\log_{10}(d_{mk,3D}) + 20\log_{10}(f_c)$ and $\mathrm{PL}_2 = 32.4 + 40\log_{10}(d_{mk,3D}) + 20\log_{10}(f_c) - 9.5\log_{10}((d_{BP}^{'})^2 + (h_{RU} - h_{UE})^2)$. $d_{mk,2D}$ is the distance between the bottom of the k^{th} UE and the m^{th} RU while $d_{mk,3D}$ denotes the distance between the top of both antennas. $d_{BP}^{'} = 4(h_{RU} - h_E)(h_{UE} - h_E)f_c/c$ represents the breakpoint distance, where $h_E = 1$ m is the effective environment height. Note that f_c is in Hz only for this equation, and c is the propagation velocity in free space. The standard deviation of shadow fading $\sigma_{SF} = 7.82$ dB [1].

C. Parameters and Setup

For generating the BLER plots, the UE positions were initially randomized but then fixed across all simulations, as depicted in Fig. 5. The simulation setup considers a square area of $100\mathrm{m} \times 100\mathrm{m}$, where 2 UEs are served by multiple RUs. Specifically, for configurations with 2 RUs, only RU1 and RU2 are utilized, while the first four RUs are selected for the 4 RU case. When comparing with co-located MIMO, we assume that the base station (BS), as shown in this figure, is equipped with 2, 4, or 8 antennas. The small-scale fading channel parameters and the fundamental setup for the PUSCH chain are outlined in Table I. Furthermore, the MCSs employed in the simulations, which are selected from [21], are listed in Table II. It's worth

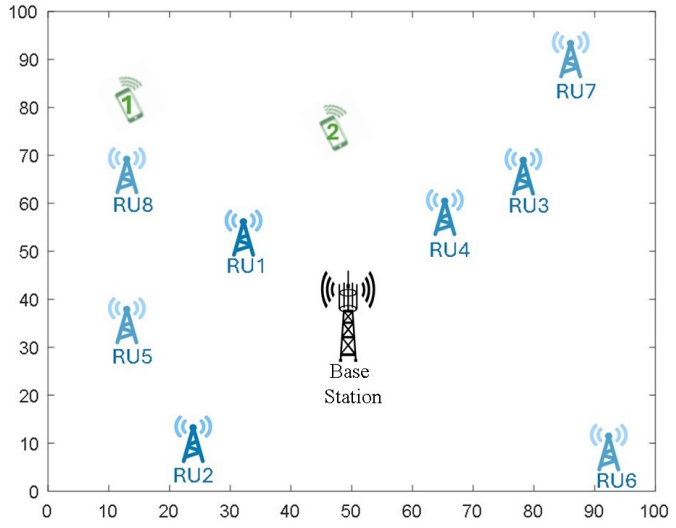

Fig. 5. A system setup with fixed locations for a BS, UEs, and RUs within a $100\text{m} \times 100\text{m}$ simulation area. UEs are serviced either by the distributed RUs (2 RUs, or 4 RUs or 8RUs) or the collocated antennas (2 or 4 or 8 antennas) at BS.

mentioning that each MCS level corresponds to a different combination of modulation order and LDPC coding rate. In our previous work [24], we've evaluated required SINR for given BLER on the AWGN channel by extensive link simulations using the range of 5G NR MCSs. This consistent setup ensures comparability across all scenarios and results.

TABLE I
SYSTEM PARAMETERS FOR THE SIMULATION

Parameters	Values
Subcarrier spacing (SCS)	15/ 30/ 60/ 120 (kHz)
Noise figure	9 dB
Noise temperature	290 K
Delay profile	TDL-B
Delay spread	30 ns
Doppler shift	0 Hz

D. Analysis and Demonstration of Results for Different MCS

Fig. 6 presents the BLER versus TX-SNR curves for a CF-MIMO system with 8 RUs and 2 UEs, illustrating the performance across a range of MCS. The two subplots represent the performance for **UE 1** and **UE 2**, respectively, covering MCS indices from 0 to 18, mapped to specific modulation schemes: QPSK (indices 0–6), 16-QAM (indices 7–10), 64-QAM (indices 11–14), and 256-QAM (indices 15–18). Each set of curves demonstrates the BLER's dependence on TX-SNR, highlighting the trade-off between SNR requirements and modulation efficiency.

In the *top subplot*, representing UE 1, the QPSK-based MCS (0–6) achieves robust performance at low TX-SNR values (72–87 dB) with acceptable BLER, albeit at lower spectral efficiency. As the MCS increases, transitioning to 16-QAM (indices 7–10) and 64-QAM (indices 11–14), the required TX-SNR for achieving BLER $< 10^{-2}$ progressively shifts toward higher values, reflecting the higher SNR demand for these

TABLE II
MCS AND TBS CONFIGURATION IN THIS PAPER

MCS	Modulation Scheme	Code Rate	PRBs	TBS
0	QPSK	30	25	208
1	QPSK	64	25	456
2	QPSK	120	25	848
3	QPSK	193	25	1352
4	QPSK	308	25	2152
5	QPSK	526	25	3752
6	QPSK	679	25	4736
7	16QAM	340	25	4736
8	16QAM	434	25	6016
9	16QAM	553	25	7808
10	16QAM	658	25	9224
11	64QAM	438	25	9224
12	64QAM	517	25	11016
13	64QAM	616	25	13064
14	64QAM	772	25	16392
15	256QAM	682.5	25	18960
16	256QAM	754	25	21000
17	256QAM	841	25	23568
18	256QAM	948	25	26632

more spectrally efficient modulations. Finally, for 256-QAM (indices 15–18), the TX-SNR requirement further increases (105–115 dB), emphasizing the trade-off for achieving maximum spectral efficiency under favorable channel conditions. Similarly, in the *bottom subplot* for UE 2, the trends follow a comparable pattern, with slight variations due to channel differences between the two UEs. The smooth decline of BLER curves across all modulation schemes demonstrates the CF-MIMO system's reliability and adaptability to varying channel conditions and user requirements. As shown in Figure 5, UE 1 is located closer to the RUs, particularly RU 8, which provides slightly better performance results compared to UE 2. This is evident at comparable TX-SNR points; for instance, at TX-SNR = 69 dB and MCS 0, UE 1 achieves a BLER of 0.14, whereas UE 2 reaches a BLER of 0.42. Similarly, at TX-SNR = 108 dB and MCS 18, UE 1 achieves a BLER of 0.07, while UE 2 requires the same TX-SNR to reach a BLER of 0.14. This proximity leads to improved channel quality, enabling lower BLER values at equivalent TX-SNR levels, as reflected in the curves for UE 1. The figure effectively showcases the scalability of the CF-MIMO system's performance across a wide range of SNR values and modulation schemes, reinforcing its suitability for diverse uplink scenarios with heterogeneous user requirements.

E. Evaluating the Impact of Practical Channel Estimation on BLER curves

Fig. 7 illustrates the BLER-SNR performance of the CF-MIMO system for UE 1 and UE 2, focusing on the impact of practical channel estimation compared to perfect channel knowledge. The performance is evaluated for selected MCS indices, specifically MCS 2, 8, 13, and 15, covering modulation schemes from QPSK to 256-QAM. The solid lines represent the results with perfect channel estimation, while the dashed lines reflect the performance under practical channel estimation. This figure demonstrates the CF-MIMO system's operation in more realistic scenarios by incorporating the effects of practical channel estimation, which introduces

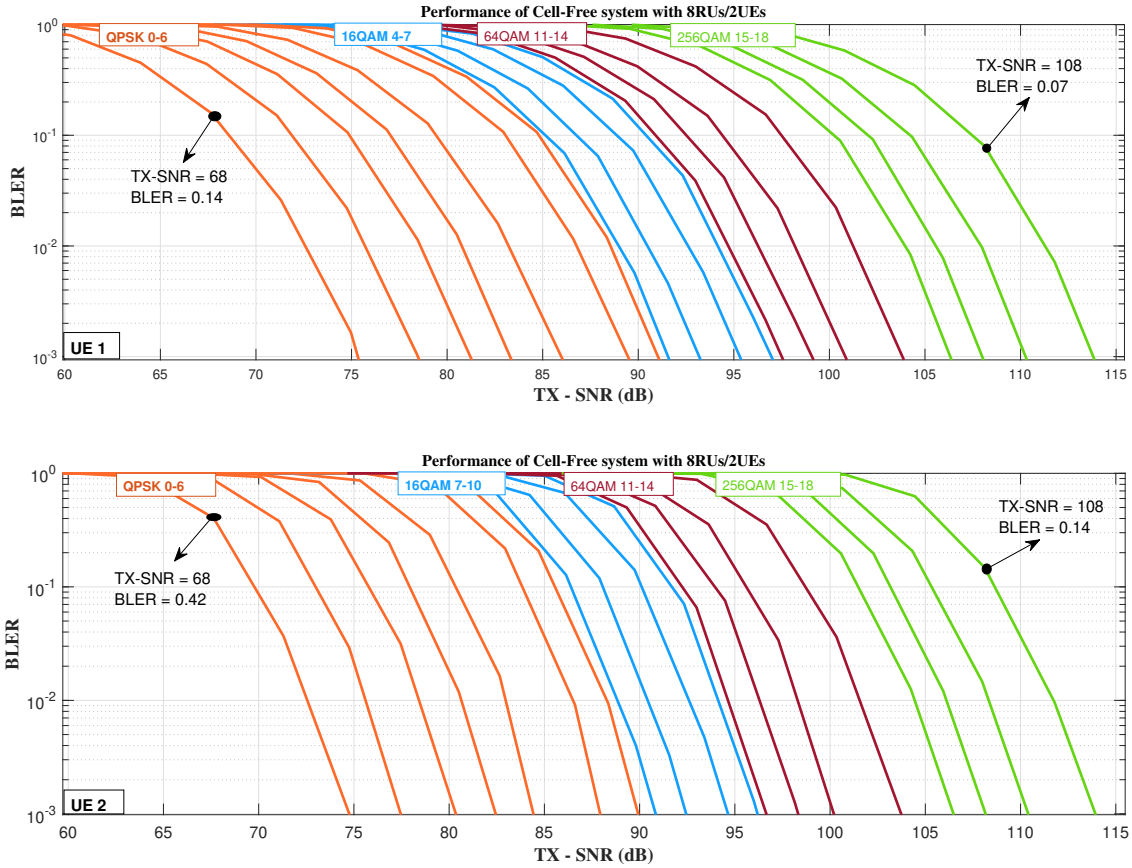

Fig. 6. BLER-SNR curves for MCS 0-18 (left to right) for CF-MIMO system with 8 RUs and 2 UEs.

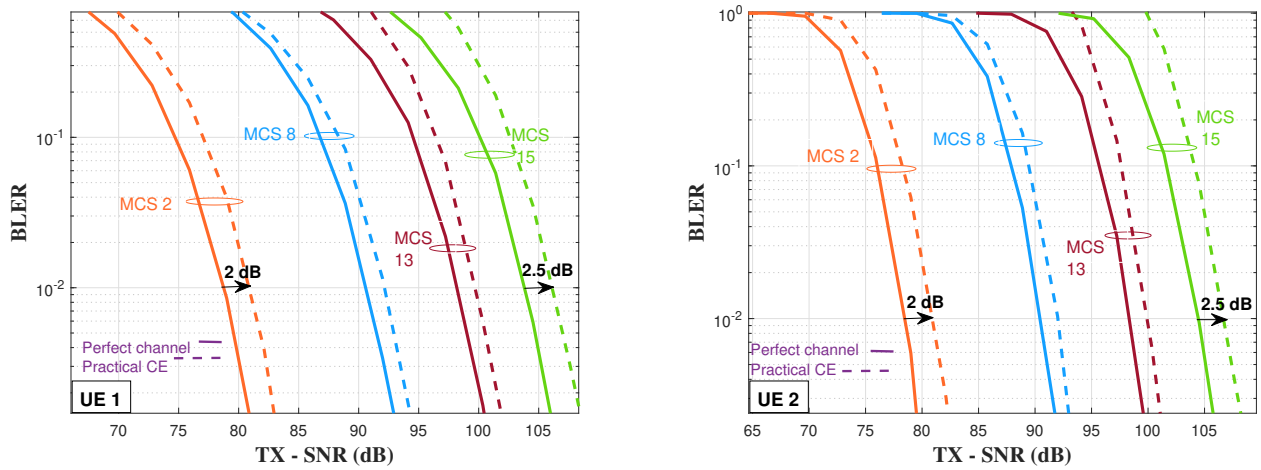

Fig. 7. BLER versus TX-SNR curves for UE1 (a) and UE2 (b) with different MCS (MCS 2, 8, 13, and 15), comparing performance under perfect channel conditions and practical channel estimation (CE).

additional imperfections due to noise and limited estimation accuracy.

For both UEs, it is evident that practical channel estimation results in a slight degradation in performance compared to the ideal case, as indicated by the horizontal shift of the BLER curves towards higher TX-SNR values, with an approximate difference of 2 dB. This degradation is more pronounced for 256-QAM, where the difference is approximately 2.5 dB, as higher modulation orders are inherently more sensitive to channel imperfections. Despite this, the CF-MIMO system maintains a reliable performance under practical channel estimation, with BLER values converging to acceptable levels as the TX-SNR increases. This indicates the system's robustness and suitability for deployment in real-world environments where perfect channel knowledge is not available. The comparison between UE 1 and UE 2 further

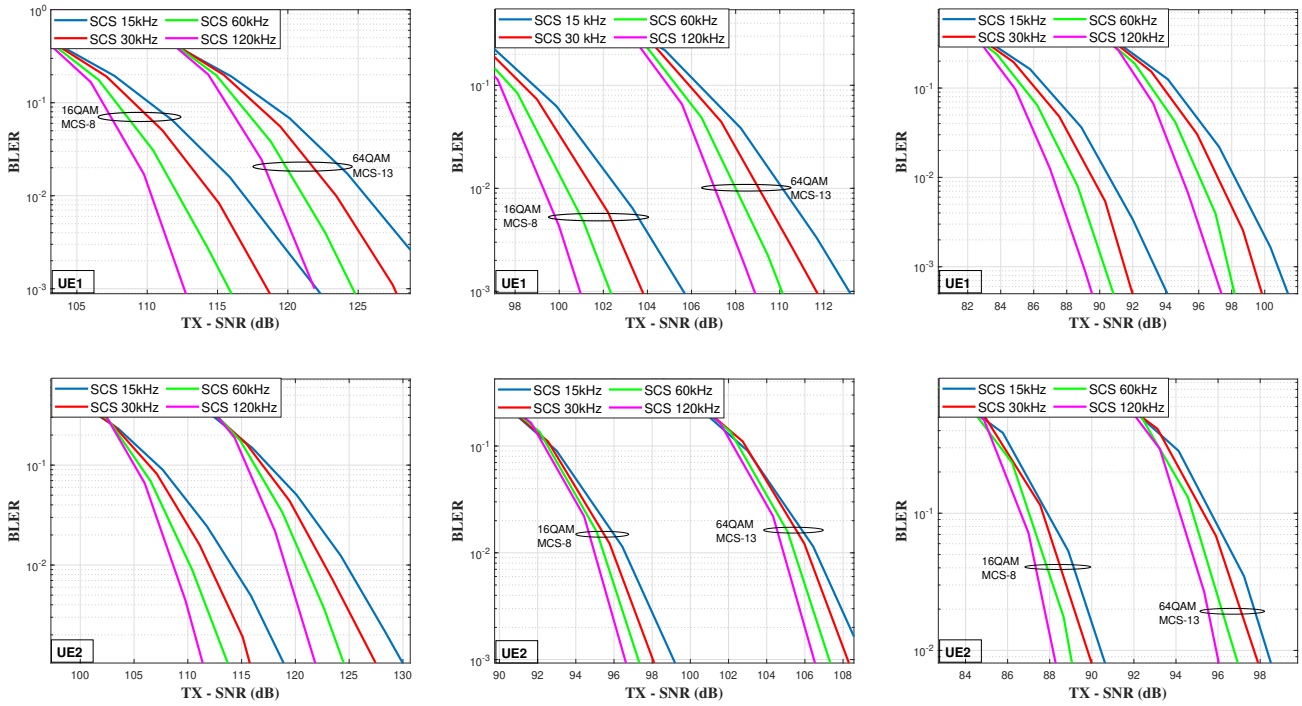

(a) Configuration 1 with 2RUs (b) Configuration 2 with 4RUs (c) Configuration 3 with 8RUs

Fig. 8. BLER versus TX-SNR curves for UE1 (top plot) and UE2 (lower plot) with MCS 8 (16-QAM) and MCS 13 (64-QAM) across three configurations (2 RUs, 4 RUs, and 8 RUs) and four subcarrier spacings (15 kHz, 30 kHz, 60 kHz, and 120 kHz), showcasing the combined effects of RU deployment and SCS on system performance and frequency diversity.

highlights the channel-dependent variations in performance, reinforcing the importance of effective channel estimation in CF-MIMO systems. In [20], the use of DMRS is comprehensively explained, highlighting the four different types of DMRS configurations based on their density and length. In this work, we specifically focus on one particular DMRS configuration for our analysis. However, we believe that there is significant potential for further exploration in this area. Future studies could investigate the performance of different DMRS configurations in various scenarios, particularly in the context of CF-MIMO systems. This includes analyzing the impact of DMRS density and length under varying channel conditions, such as high Doppler shifts and different delay spread profiles, which are common in practical environments. Extending this work to include such considerations would provide deeper insights into the optimization of DMRS configurations and their effect on system performance in CF deployments, and we plan to explore these aspects in our future research.

F. Evaluating the Effect of Signal Bandwidth by Varying Subcarrier Spacing from 15 to 120 kHz

Fig. 8 illustrates the impact of SCS on the performance of the CF-MIMO system, focusing on the bandwidth of the transmitted signals. The results are shown for the perfect channel estimation scenario, providing a baseline for evaluating the effect of different SCS values on system performance. The BLER-SNR performance is evaluated for two modulation and coding schemes (MCS 8 and 13) and for three system configurations (2 RUs, 4 RUs, and 8 RUs) with four different SCS values: 15 kHz, 30 kHz, 60 kHz, and 120 kHz. By increasing the SCS from 15 kHz to 120 kHz, the bandwidth of the signals increases proportionally, ranging from 4.5 MHz to 36 MHz. Given the channel's delay spread of 30 ns, the approximate coherence bandwidth is 5.5 MHz, which plays a critical role in understanding the system's frequency diversity.

As evident in the figure, increasing the SCS improves performance due to enhanced frequency diversity. When the SCS exceeds the coherence bandwidth (e.g., 30 kHz, 60 kHz, and 120 kHz), multiple subcarriers experience uncorrelated fading, allowing the system to leverage frequency diversity. This results in improved reliability and lower BLER at a given TX-SNR. For both UE 1 and UE 2, the trends confirm these conclusions, with higher SCS values consistently leading to steeper BLER curves and reduced TX-SNR requirements for achieving low BLER levels. Moreover, the effect of increasing SCS is observed across all configurations. In Configuration 3 (with 8 RUs), the performance improvement is particularly pronounced due to better spatial diversity in combination with frequency diversity. The consistency of this trend across both UEs underscores the robustness of the CF-MIMO system in exploiting frequency diversity through higher SCS values. This analysis highlights the importance of matching the SCS to the channel conditions, particularly the coherence bandwidth, to maximize system performance.

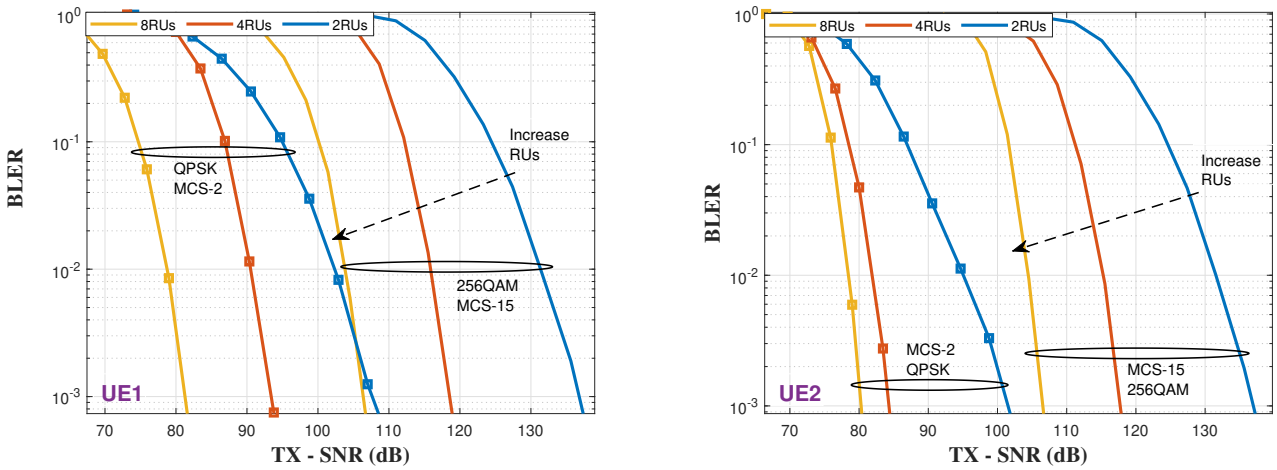

Fig. 9. BLER versus TX-SNR performance for UE1 and UE2 with varying numbers of RUs (2, 4, and 8) for MCS 2 (QPSK) and MCS 15 (256-QAM), highlighting the impact of increased RUs on spatial diversity and proximity to RUs

G. Evaluating the Effect of Varying the Number of RUs on BLER

Figure 9 highlights the impact of increasing the number of RUs on the BLER-SNR performance for UE 1 and UE 2. Increasing the number of RUs offers two key benefits: (1) enhanced spatial diversity, which improves reliability by utilizing multiple propagation paths, and (2) an increased likelihood of a UE being physically closer to one or more RUs, a phenomenon often referred to as "site diversity" [25], resulting in better channel conditions and improved overall performance. By examining the RU locations in the accompanying layout (5), it is evident how the spatial configuration affects the performance of each UE differently.

For UE 2, increasing the number of RUs from 2 to 4 results in significant improvement due to its proximity to RUs in the 4-RU configuration, particularly RU 4. This closer proximity reduces path loss and enhances signal quality, which is clearly reflected in the performance improvement from 2 RUs to 4 RUs. However, for UE 1, the most noticeable improvement occurs when the number of RUs increases from 4 to 8. In the 8-RU configuration, UE 1 becomes significantly closer to RU 8, leveraging site diversity, where the specific spatial arrangement of RUs relative to UEs offers additional diversity gains. This trend illustrates that the benefits of adding RUs are configuration-dependent, with different UEs experiencing varying degrees of diversity improvement based on their relative location to the RUs.

For both UEs, increasing the number of RUs from 2 to 4 results in steeper BLER curves, indicating enhanced spatial diversity. In contrast, increasing the number of RUs from 4 to 8 shifts the curves to the left without affecting their slope, as the improvement is primarily attributed to enhanced site diversity. This analysis underscores the importance of spatial diversity and proximity in CF-MIMO systems, with each configuration offering unique advantages for different UEs. Exploring this concept further, particularly the interplay between site diversity and system configuration, will be a key focus of our future work to optimize performance under diverse deployment scenarios.

H. Impact of Co-Located vs Distributed Antenna Configurations on BLER

Figure 10 examines the BLER-SNR performance for UE 1 and UE 2, focusing on the differences between co-located and distributed antenna configurations under MCS 8 (16QAM) with varying numbers of antennas (2, 4, and 8). While the co-located configuration centralizes all antennas at the BS, the distributed configuration, as shown in Fig. 5, employs spatially distributed RUs, each equipped with one antenna. For 2 antennas, it can be observed that the co-located configuration performs better for both UE 1 and UE 2, with a more significant performance gap observed for UE 2. This difference can be attributed to the specific locations of the UEs, RUs (RU1 and RU2), and the BS. In this case, the co-located configuration benefits from centralized processing at the BS, which provides stronger and more consistent signals to both UEs compared to the distributed setup with only two RUs.

As the number of antennas increases from 2 to 8, the distributed configuration shows significant improvement in performance for both UEs, with the BLER curves shifting to lower SNR values. However, for the co-located setup with 8 antennas, the curve becomes steeper than that of the distributed configuration. This is because the spatial diversity in the co-located case is higher with all antennas centrally aggregated, resulting in more effective multi-antenna processing for the UEs located nearby.

It is important to note that these results are specific to the current setup, including the locations of UEs, RUs, and the BS. The performance trends would change if these locations were altered. For instance, in different setups, the distributed configuration may show advantages for UE 1 even with 2 antennas, depending on the relative positions of UEs and RUs. These results underscore the importance of considering deployment geometry when evaluating the performance of CF-MIMO systems.

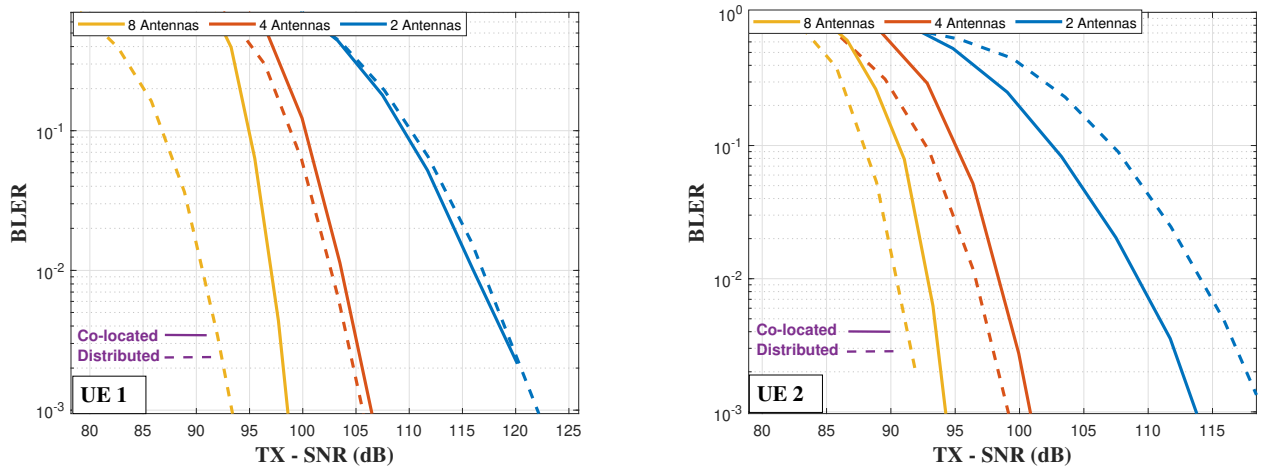

Fig. 10. BLER versus TX-SNR performance for UE1 and UE2 with varying numbers of antennas (2, 4, and 8) for MCS 8 (16QAM), comparing the performance of the co-located and distributed configurations

V. Future Work and Discussion

Future work will extend our link-level simulation to encompass the downlink scenario, focusing on a comprehensive evaluation of CF-MIMO systems. This will include the incorporation of multi-antenna RUs transmitting multi-layer streams. Additionally, we aim to investigate channel estimation under challenging conditions, such as high Doppler shifts, varying delay spreads, and pilot contamination caused by pilot reuse, with a focus on designing robust DMRS configurations to address these challenges. Furthermore, we plan to explore RU and shadow fading correlation, along with developing advanced algorithms for RU placement to enhance site diversity. To ensure more representative and generalizable results, we will consider using a more realistic RU/UE layout, such as a hexagonal RU arrangement or analyzing statistics over fully random RU and UE placements. Finally, evaluations in complex environments with heterogeneous user distributions, mobility, and inter-cell interference will validate the scalability and practicality of CF-MIMO systems.

VI. Conclusion

In this work, we have analyzed the performance of CF-MIMO systems across various configurations and parameter settings, including the number of RUs, SCS, MCS, and the effects of practical versus perfect channel estimation. Notably, this study is grounded in 5G NR assumptions and considers frequency-selective channels, an approach that is rare, if not unique, in the existing literature. Our findings highlight the substantial influence of these parameters on system performance, providing valuable insights for optimizing CF-MIMO systems to meet the demands of real-world deployments.

The results demonstrate that increasing the number of RUs enhances spatial diversity and proximity benefits, while higher SCS values leverage frequency diversity, particularly for bandwidths exceeding the channel's coherence bandwidth. Additionally, practical channel estimation confirms the system's robustness under realistic conditions. The concept of site diversity, introduced by specific RU configurations, underscores the importance of tailored deployment strategies for maximizing diversity and reliability across diverse UEs.

This study lays a solid foundation for advancing CF-MIMO systems, emphasizing their potential to transform wireless communication with unparalleled reliability and flexibility in various deployment scenarios.

References

[1] E. Björnson and L. Sanguinetti, "Scalable cell-free massive MIMO systems," *IEEE Transactions on Communications*, vol. 68, no. 7, pp. 4247–4261, 2020.

[2] X. Lin, J. Li, R. Baldemair, J.-F. T. Cheng, S. Parkvall, D. C. Larsson, H. Koorapaty, M. Frenne, S. Falahati, A. Grovlen *et al.*, "5G new radio: Unveiling the essentials of the next generation wireless access technology," *IEEE Communications Standards Magazine*, vol. 3, no. 3, pp. 30–37, 2019.

[3] Ö. T. Demir, E. Björnson, L. Sanguinetti *et al.*, "Foundations of user-centric cell-free massive MIMO," *Foundations and Trends® in Signal Processing*, vol. 14, no. 3-4, pp. 162–472, 2021.

[4] F. Göttsch, N. Osawa, T. Ohseki, K. Yamazaki, and G. Caire, "Subspace-based pilot decontamination in user-centric scalable cell-free wireless networks," *IEEE Transactions on Wireless Communications*, vol. 22, no. 6, pp. 4117–4131, 2022.

[5] ——, "The impact of subspace-based pilot decontamination in user-centric scalable cell-free wireless networks," in *2021 IEEE 22nd International Workshop on Signal Processing Advances in Wireless Communications (SPAWC)*. IEEE, 2021, pp. 406–410.

[6] M. Rahmani, M. Bashar, M. J. Dehghani, A. Akbari, P. Xiao, R. Tafazolli, and M. Debbah, "Deep reinforcement learning-based sum rate fairness trade-off for cell-free mMIMO," *IEEE Transactions on Vehicular Technology*, vol. 72, no. 5, pp. 6039–6055, 2022.

[7] J. Zheng, J. Zhang, E. Björnson, and B. Ai, "Impact of channel aging on cell-free massive MIMO over spatially correlated channels," *IEEE Transactions on Wireless Communications*, vol. 20, no. 10, pp. 6451–6466, 2021.

[8] W. Jiang and H. D. Schotten, "Impact of channel aging on zero-forcing precoding in cell-free massive MIMO systems," *IEEE Communications Letters*, vol. 25, no. 9, pp. 3114–3118, 2021.

[9] G. Femenias and F. Riera-Palou, "Cell-free massive MIMO-OFDM over spatially correlated doubly selective channels," *IEEE Access*, vol. 10, pp. 118 438–118 453, 2022.

[10] W. Jiang and H. D. Schotten, "Opportunistic AP selection in cell-free massive MIMO-OFDM systems," in *IEEE 95th Vehicular Technology Conference*. IEEE, 2022, pp. 1–5.

[11] J. Zheng, J. Zhang, E. Björnson, Z. Li, and B. Ai, "Cell-free massive MIMO-OFDM for high-speed train communications," *IEEE Journal on Selected Areas in Communications*, vol. 40, no. 10, pp. 2823–2839, 2022.

[12] W. Jiang and H. D. Schotten, "Cell-free massive MIMO-OFDM transmission over frequency-selective fading channels," *IEEE Communications Letters*, vol. 25, no. 8, pp. 2718–2722, 2021.

[13] H. Ge, N. Garg, and T. Ratnarajah, "Channel estimation for generalized superimposed cell-free massive MIMO-OFDM systems," in *2022 IEEE 23rd International Workshop on Signal Processing Advances in Wireless Communication (SPAWC)*. IEEE, 2022, pp. 1–5.

[14] Y. Al-Eryani, M. Akrout, and E. Hossain, "Multiple access in cell-free networks: Outage performance, dynamic clustering, and deep reinforcement learning-based design," *IEEE Journal on Selected Areas in Communications*, vol. 39, no. 4, pp. 1028–1042, 2020.

[15] S. Kurma, K. Singh, P. K. Sharma, C.-P. Li, and T. A. Tsiftsis, "On the performance analysis of full-duplex cell-free massive mimo with user mobility and imperfect csi," *IEEE Transactions on Communications*, 2024.

[16] Y. Kabalcı and M. Ali, "Throughput analysis over 5G NR physical uplink shared channels," in *2020 2nd Global Power, Energy and Communication Conference (GPECOM)*. IEEE, 2020, pp. 345–349.

[17] G. Cisek and T. P. Zieliński, "Prototyping software transceiver for the 5G new radio physical uplink shared channel," in *2019 Signal Processing Symposium (SPSympo)*. IEEE, 2019, pp. 150–155.

[18] V. Ranjbar, A. Girycki, M. A. Rahman, S. Pollin, M. Moonen, and E. Vinogradov, "Cell-free mMIMO support in the O-RAN architecture: A PHY layer perspective for 5G and beyond networks," *IEEE Communications Standards Magazine*, vol. 6, no. 1, pp. 28–34, 2022.

[19] "Technical Specification Group Radio Access Network; NR; Physical channels and modulation," 3rd Generation Partnership Project (3GPP), Technical Specification TS 38.211, 2017, release 15.

[20] "5G NR, Physical channels and modulation," 3rd Generation Partnership Project (3GPP), Technical Report TR 38.211, 2020, release 16.

[21] "Study on channel model for frequencies from 0.5 to 100 GHz," 3rd Generation Partnership Project (3GPP), Technical Report TR 38.901, 2022, release 17.

[22] "LTE; Evolved Universal Terrestrial Radio Access (E-UTRA); Physical channels and modulation," 3rd Generation Partnership Project (3GPP), Technical Specification TS 36.211, 2016, release 14.

[23] "User Equipment (UE) Radio Transmission and Reception," 3rd Generation Partnership Project (3GPP), Technical Specification TS 36.101, 2016, release 15.

[24] L. Méndez-Monsanto, A. MacQuarrie, M. R. Ghourtani, M. J. L. Morales, A. G. Armada, and A. Burr, "BLER-SNR curves for 5G NR mcs under AWGN channel with optimum quantization," in *2024 IEEE 100th Vehicular Technology Conference (VTC2024-Fall)*. IEEE, 2024, pp. 1–6.

[25] D. A. Basnayaka, P. J. Smith, and P. A. Martin, "Performance analysis of macrodiversity mimo systems with mmse and zf receivers in flat rayleigh fading," *IEEE transactions on wireless communications*, vol. 12, no. 5, pp. 2240–2251, 2013.